ORIGINAL PAPER

Inorganic-based sol–gel synthesis of nano-structured LiFePO$_4$/C composite materials for lithium ion batteries

Jun Ma · Baohua Li · Hongda Du · Chengjun Xu · Feiyu Kang

Abstract An inorganic and non-toxic compounds combination of FeCl$_2$·4H$_2$O, Li$_2$CO$_3$ and H$_3$PO$_4$ was chosen to synthesize homogeneous nano-structured LiFePO$_4$/C composite material via a simplified sol–gel route. The dependency of the physicochemical properties and the corresponding electrochemical responses on the residual carbon content were investigated in details. Rietveld refinement of X-ray diffraction measurement and X-ray photoelectron spectroscopy analysis confirmed the feasibility of preparing pure LiFePO$_4$ phase via this approach. With increasing amount of residual carbon, the particles size gradually decreased and the bulk electrical conductivity monotonically increased. However, the higher level of residual carbon would bring disadvantageous impact on the lithium ion diffusion. Due to high electrical conductivity, controlled particle size and suitable microstructure, the sample with 4.5 wt.% residual carbon exhibited stable cycling performance and delivered high discharge capacity of 163, 119 and 108 mA hg^{-1} at 0.1 C, 5 C and 10 C, respectively.

Keywords Lithium-ion battery · Inorganic compounds · LiFePO$_4$/C · Sol–gel route · In situ carbon coating

J. Ma · B. Li · H. Du · C. Xu
Advanced Materials Institute, Graduate School at Shenzhen,
Tsinghua University,
Shenzhen, Guangdong Province 518055, China

J. Ma · F. Kang (✉)
Laboratory of Advanced Materials, Department of Materials
Science and Engineering, Tsinghua University,
Beijing, 100084, China
e-mail: fykang@tsinghua.edu.cn

Introduction

Much attention has been focused on the development of new-generation cathode materials to replace commercial LiCoO$_2$ due to its toxicity, cost and safety problem. Subsequently, many alternative cathode materials [1, 2] have been exploited successively, inclusive of LiFePO$_4$ [3]. As a particularly appealing and promising cathode material for lithium-ion batteries, especially for hybrid energy storage and pure electric systems where cost and safety are of major concerns [4], LiFePO$_4$ exhibits many unique features, such as low cost, relative abundant resource, environmental compatibility, high theoretical capacity (~170 mA hg^{-1}), suitable charge/discharge plateau voltage (~ 3.45 V vs. Li), long life span, excellent thermal and stability in the fully charged state [3, 5]. However, this electrode material is quite eclipsed by its intrinsic flaws. LiFePO$_4$ itself is in essence a mixed ionic–electronic conductor [6]. It possesses sluggish lithium ion diffusion (10^{-13} to 10^{-16} cm^2 s^{-1}) [7] and poor electronic conductivity (~10^{-9} cm s^{-1}), which dramatically hinder the transport of lithium-ion and electron within the lattice. For this reason, LiFePO$_4$ can deliver the relative higher specific capacity only at the extremely small current density. Quite obviously, it is difficult to satisfy the practical requirements for high-energy and high-power densities. In the light of these serious disadvantages, extensive research efforts have been made. The corresponding strategies mainly involve in optimizing powder morphology, tailoring the crystallite size, decorating the surface with conductive agents [8–10], depositing in carbonaceous matrix [11–14], doping with alien cations on the Li ion site or/and Fe ion site [4, 15–20] and recently anions doping (e.g., Cl$^-$ and F$^-$) on the O ion site [21–23].

However, whatever strategy is taken, both the reasonable selection of preparation procedure and the optimal combination of raw materials are of always paramount importance. Up to now, there has been a variety of synthetic methods proposed to prepare $LiFePO_4$ powder with excellent physicochemical and electrochemical properties. Generally speaking, these approaches can be roughly divided into three categories: conventional solid-state chemistry, solution chemistry and other synthesis routes [24–38]. By comparison with other synthesis procedures, the sol–gel process is regarded as a deliberate choice because this method can easily ensure high purity and homogeneity, effectively control morphology and particle size, and be convenient to the subsequent bulk doping and/or in situ carbon coating.

In recent years, little progresses and innovations have been made in terms of synthesizing $LiFePO_4$ via the sol–gel route. For the purpose of the sol–gel synthesis of $LiFePO_4$, toxic and expensive organic iron salts or/and lithium salts were usually selected as raw materials, such as $FeCl_2 \cdot 4H_2O$ and $CH_3CO_2Li \cdot H_2O$ [24], $Fe(acac)_3$ and $LiOH \cdot H_2O$ [33], $FeC_2O_4 \cdot 2H_2O$ and Li_2CO_3 [35], $Li_2(C_2O_4)$ and $FeC_2O_4 \cdot 2H_2O$ [36]. Undoubtedly, production costs would be dramatically increased and the environment would be seriously threatened, which would greatly weaken the advantages of this approach and make it unfavorable to large-scale applications. In order to alleviate these deficiencies, it is urgent to replace theses organic alkoxides. There are a limited number of literatures concerning about inorganic compounds as raw materials. Croce et al. [37] selected lithium hydroxide monohydrate ($Li(OH \cdot H_2O)$), ferric nitrate ($Fe(NO_3)_3$) and phosphoric acid (H_3PO_4) to synthesize $LiFePO_4$ with high rate capability. Later, Li et al. [38] successfully prepared $LiFePO_4$ by using ferrous chloride tetrahydrate ($FeCl_2 \cdot 4H_2O$), lithium chloride monohydrate ($LiCl \cdot H_2O$) and phosphoric acid (H_3PO_4) as raw materials. However, in these cases, $Fe(NO_3)_3$ will pose a potential menace to health, meanwhile $LiCl \cdot H_2O$ is apt to absorb the moisture from air and low toxicity. Therefore, it is of necessity and practical significance to seek for another alternative combination of the non-toxic and cheap inorganic compounds as raw materials and investigate their feasibility further.

In addition, sol–gel synthesis is generally complex and time consuming. The gelation process of sol needed to be assisted by heating and solvent (usually water) has to be evaporated at high temperatures (e.g., 150 °C). The desiccating of gel is required to be carried out under high-pure Ar gas protection in order to avoid the oxidation of ferrous ions to an extreme degree. In some cases, additional follow-up treatments were required. For example, Sanchez et al. [33] reported that the precursor was centrifuged and then washed with organic solution so as to remove harmful

impurities. Last but not least, when ferric salts was used, the precursor synthesis would inevitably involve the reduction of Fe^{3+} by reducing agent (e.g., ascorbic acid, aniline) and the adjustment of pH by ammonia water [37]. Undoubtedly, these steps added cost, extended processing time and enhanced the complexity of the process, which are some of the reasons why the sol–gel synthesis route cannot be applied widely. Therefore, it is necessary to make some effective measurements to overcome these disadvantageous factors.

In this paper, we explore a cheap and simplified sol–gel method to synthesize nano-crystallite $LiFePO_4$/C composite electrode with improved electrochemical performance. For the first time, we selected a cheap and nontoxic inorganic compounds combination ($FeCl_2 \cdot 4H_2O$, Li_2CO_3 and H_3PO_4) as raw materials. During the preparation of the precursor, the gelation process occurs spontaneously without heating and pH value is not adjusted. The evaporation of solvent (ethanol) is carried out at a low temperature for a very short time without any additional protection. The results indicate that the sample with 4.5 wt.% residual carbon presented excellent rate capability and cycling stability. This inorganic-based sol–gel synthesis displays a great potential for large-scale production.

Experimental

Synthesis

The $LiFePO_4$ precursor was synthesized using an inorganic compounds combination of $FeCl_2 \cdot 4H_2O$ (analytical reagent [AR], 98.5%), Li_2CO_3 (AR, 99%) and H_3PO_4 (AR, >98%) as raw materials and citric acid (AR, >99.5%) as the carbon source. According to a desired stoichiometry, all reactants were added successively into ethanol to form a blue sol, maintaining magnetic stirring. After 3 h, the chemical reaction was completed. The stirring was stopped and the pale blue gel was formed immediately. In order to accomplish in situ carbon coating, the different amounts of citric acid were added into ethanol during the preparation of precursor. For the sake of easy discussions later, we denoted the sample with adding 0.5 mol citric acid as sample A, 1 mol citric acid as sample B and 2 mol citric acid as sample C. After being dried at 85 °C for overnight, the as-obtained green xerogel was pre-calcined at 350 °C for 5 h under Ar gas atmosphere, followed by final calcinination at 650 °C for 15 h in flowing Ar gas in tube furnace.

Physicochemical characterization

A Rigaku D/max 2500/PC diffractometer was used to obtain X-ray powder diffraction patterns for the samples

using Cu Kα radiation. The diffraction data were collected at step mode over the angular range of 15–120° with a step size 0.02° and a 5-s exposure time at 50 kV, 250 mA. The crystal structure parameters for samples were refined by Rietveld analysis using Maud program. A *Pnma* space group was chosen as the model. The average crystallite size was calculated by a Scherrer equation from the full-width at half-maximum (FWHF) of (101), (111) or (201), (211) or (020) and (311) peaks. X-ray photoelectron spectroscopy (XPS; PHI 5600) equipped with monochromatic Al (1,486.6 eV) X-ray source was used to analyze the chemical valence states of the elements. Analysis of data was performed using the XPSPEAK processing software. All data were calibrated using adventitious C 1 s peak with a fixed value of 284.4 eV. The background from each spectrum was subtracted using a Shirley-type background. The specific surface areas of samples were measured using multi-point (eight) Brunauer–Emmett–Teller (BET) technique (Micromeritics ASAP 2020 M+C). The residual carbon content for sample was determined by a chemical analysis. A certain amount of sample was first added in the hydrochloride acid solution with a concentration of around 20 wt.% and then heated at 85 °C in order to completely dissolve the lithium iron phosphate. Secondly, the solution was filtered using a sand core funnel. The residue was repeatedly washed with dilute hydrochloride with a concentration of approximately 2.2 wt.% and deionized water, respectively. After drying, the remnant was carbon coated on the surface of the LiFePO$_4$ particles. The morphologies of samples were observed by field emission scanning electron microscopy (FESEM, Hitachi S4800) operating at 10 kV. High-resolution transmission electron microscopy (HR-TEM, JOEL JSM-2100 F) images of the samples were collected under an accelerating voltage of 200 kV. The bulk electrical conductivity for sample was measured using four point resistivity test system (SDY-4). The pellets with a diameter of 13 mm used for the electrical conductivity measurements were prepared by uniaxially pressing the LiFePO$_4$ powder with a pressure of 10 MPa.

Electrochemical characterization

The cathode was composed of the as-synthesized powder, 5 wt.% acetylene black (super P) and 5 wt.% polyvinylidene fluoride (PVDF). The loading amount of active material was about 5 mg cm^{-2}. The CR2032 coin cell with a metallic lithium anode was assembled to assess electrochemical performances. The microporous polypropylene sheet (Celgard 2500, Celgard Inc., USA) was used as a separator, 1 molar LiPF$_6$ dissolved in ethylene carbonate and diethyl carbonate (EC/DEC) solution (1:1 by volume) was used as electrolyte. The electrochemical AC impedance spectroscopy (EIS) was performed under open-circuit

voltage in the frequency range of 10 mHz to 100 kHz with an excitation amplitude of 5 mV using a Zahner Elektrik Im6ex electrochemical working station. The galvanostatic charge/discharge and cycling stability tests were performed using a Land 2001A cell test system (Wuhan, China) at room temperature.

Results and discussion

Physicochemical characterizations

Figure 1a shows the X-ray diffraction (XRD) patterns for the as-resulting LiFePO$_4$ samples with different residual carbon amounts. All XRD diffraction peaks match with the
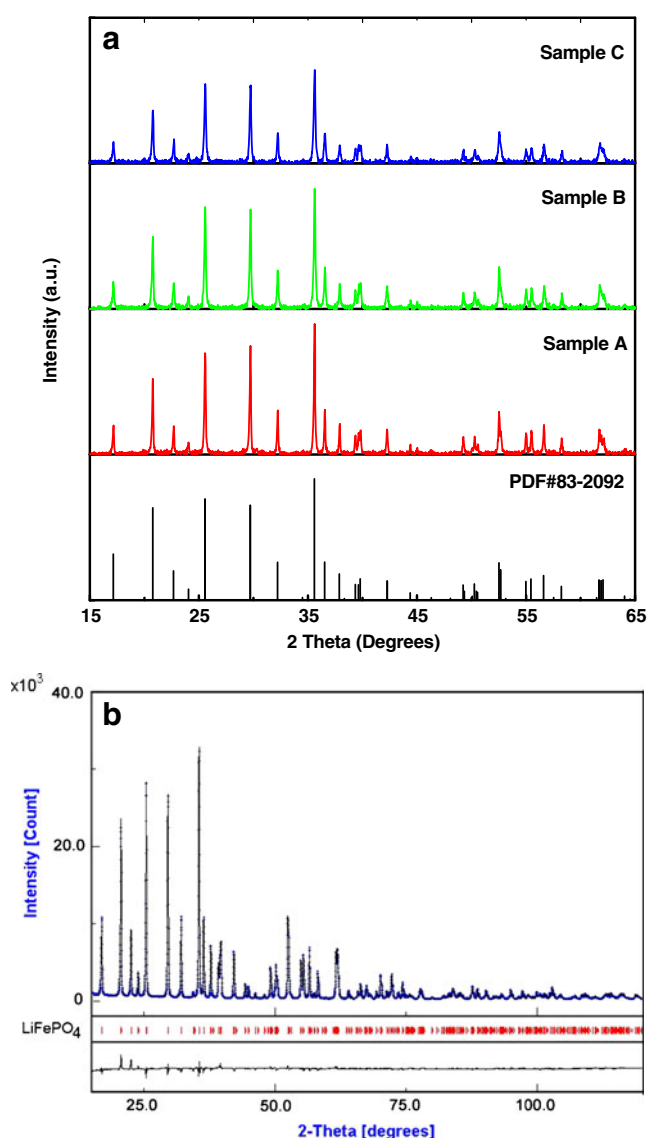

Fig. 1 **a** XRD patterns of the as-synthesized samples with different residual carbon contents. **b** Rietveld refinement pattern of sample B

standard pattern of orthorhombic LiFePO$_4$ structure very well. No odd phases, which could be assigned to Fe(III) compounds, iron carbides and iron phosphide, could be detected. The crystallographic evidence indicates that all samples synthesized by this innovative inorganic-based sol–gel approach are identified as single-phase LiFePO$_4$. In addition, the characteristic diffraction peaks corresponding to crystalline carbon could not be found, indicating that the added citric acid was pyrolyzed as amorphous carbon during the process of calcining. The XRD Rietveld refinement pattern of sample B is shown in Fig. 1b and the detailed structural parameters for all samples are listed in Table 1. The refinement results indicate that a well-crystallized stoichiometric LiFePO$_4$ phase is synthesized with lattice parameters very similar to that in JCPDS 83–2092 (Pnma 62, $a=10.334$Å, $b=6.01$Å, $c=4.693$Å). The XRD results demonstrated the feasibility of synthesizing pure LiFePO$_4$ phase via this method.

A detailed crystalline size (D) was calculated using a Scherrer equation $\beta \cos(\theta) = k\lambda/D$, where β is the half-peak width of the XRD diffraction peak and k is a constant (0.89). It was found that the average crystalline size (D) of samples A, B and C decreased from 59.6, 49.2 to 43.1 nm, whereas the specific surface area increased from 25.9, 34.5 and 56.6 m^2 g^{-1} with increasing adding amounts of citric acid. In addition, the corresponding residual carbon

contents were gauged to be 2.3, 4.5 and 15 wt.%, respectively. Apparently, the grain size was gradually reduced with the increase of the residual carbon content. This means that the introduction of amorphous carbon will be beneficial to refine the particle size. This phenomenon can be explained by the space steric effect of amorphous carbon. The space steric effect increased the diffusion activation energy of reactants and slowed down the growth rate of grains. Therefore, the more citric acid was added, the more the pyrolyzed amorphous carbon was, the more apparent this space steric effect became and thus the smaller the particle size was.

The relationship between the bulk electrical conductivity and the residual carbon content was investigated by the four-point resistivity test system. The bulk electrical conductivities of samples varied from 4.14×10^{-5}, 2.82×10^{-4} to 1.44×10^{-3} S cm^{-1} were measured at room temperature upon increasing the amount of residual carbon, respectively. Since XRD analysis has indicated the absence of the potential conductive substrates (i.e., iron phosphides or iron carbides), the improvement of the bulk electrical conductivity mainly results from the residual carbon in samples. The results showed that the bulk electrical conductivity was increased monotonically with the residual carbon content. This trend coincides with the data reported by Bewlay et al. [39]. They found that the bulk electrical

Table 1 Parameters obtained with Rietveld refinement for all samples

Sample	Sample A	Sample B	Sample C
Lattice constant (Å)			
a	10.33021(3)	10.32834(8)	10.32783(1)
b	6.00713(2)	6.00592(7)	6.00643(3)
c	4.69095(3)	4.69134(7)	4.69369(7)
Atomic position			
Li	(0, 0, 0)	(0,0,0)	(0,0,0)
Fe	(0.2823, 0.25, 0.9750)	(0.2822, 0.25, 0.9750)	(0.2822, 0.25, 0.9751)
P	(0.0948, 0.25, 0.4157)	(0.0947, 0.25, 0.4154)	(0.0946, 0.25, 0.4152)
O1	(0.1000, 0.25, 0.7487)	(0.1004, 0.25, 0.7487)	(0.1007, 0.25, 0.7492)
O2	(0.4539, 0.25, 0.2070)	(0.4537, 0.25, 0.2075)	(0.4537, 0.25, 0.2070)
O3	(0.1679, 0.0414, 0.2826)	(0.1677, 0.0414, 0.2823)	(0.1679, 0.0415, 0.2821)
Site occupancy			
Li	1	1	1
Fe	1	1	1
P	1	1	1
O1	1	1	1
O2	1	1	1
O3	1	1	1
Reliability factors			
R_{wp} (%)	9.66	7.82	8.46
R_p (%)	6.67	5.48	5.89
χ^2 (%)	2.981	2.468	2.663

conductivity was increased to about 10^{-4} S cm^{-1} when the carbon content was about 3 wt.%, while it could be raised to about 10^{-2} S cm^{-1} as the carbon content was up to approximately 23 wt.%.

The XPS full spectrum of sample B and its core XPS spectra in the binding energy range of C 1 s, O 1 s, P 2p and Fe 2p are showed in Fig. 2a–e. The XPS spectra for other samples are not given due to the similarity with the sample B. In the XPS full spectrum shown in Fig. 2a, the peaks corresponding to elements Fe, P, O and C were found, which indicated the presence of elements Fe, P, O and C on the surface of sample. However, the characteristic peak ascribed to element Cl was not observed, indicating the absence of element Cl. It means that the impurity element Cl introduced as raw material could be removed by calcining. As shown in Fig. 2b, the asymmetric peak of the C 1 s line was found at approximately 284.4 eV, which indicated the presence of amorphous carbon. The result is in good agreement with the analysis results obtained by XRD. The O 1 s core XPS peak (Fig. 2c) at about 531.4 eV in the spectra was attributed to oxygen atoms of $(PO_4)^{3-}$ group. In addition, it was found that the P 2p spectrum (Fig. 2d) was split into two components ($2p_{3/2}$ and $2p_{1/2}$) due to spin–orbit coupling (at 133.2 and 134 eV, respectively). The sample only shows one P chemical state, i.e., $(PO_4)^{3-}$. The result further indicates the absence of iron phosphides, which accords with that of XRD. Lastly, the Fe 2p spectrum (Fig. 2e) is composed of two main peaks and their satellite peaks at higher binding energies [40]. The appearance of satellite peaks or shoulder peaks is a characteristic feature of transition metal ions with partially filled d-orbits. A Fe $2p_{3/2}$ main peak is at 710.6 eV with its satellite peak at 714 eV and a Fe $2p_{1/2}$ main peak is at 724.1 eV with its satellite peak at 727.4 eV. The spin-orbital split energy (Δ) is about 13.5 eV. The values are in good agreement with that of Fe^{2+} ions. This means that the chemical oxidation state of Fe is +2. Although $FeCl_2 \cdot 4H_2O$ is apt to hydrolyze to form ferric salts, Fe^{3+} ion was not found in the final product. The results further validated the feasibility of synthesizing LiFePO$_4$/C composite materials by this innovative inorganic-based sol–gel route.

Figure 3 shows SEM micrographs of the platinum sputtered LiFePO$_4$/C samples. The photographs clearly show the differences in micromorphologies of the LiFePO$_4$/C powders with different residual carbon contents. As shown in Fig. 3a, sample A contains near-spherical particles of various sizes, which varies from few hundred nanometers to few tens of nanometer. Sample B (Fig. 3b) shows that spherical particles with uniform particle size (~71 nm) are interconnected to form porous and loose network structure by the pyrolyzed amorphous carbon. This porous and loose structure would be
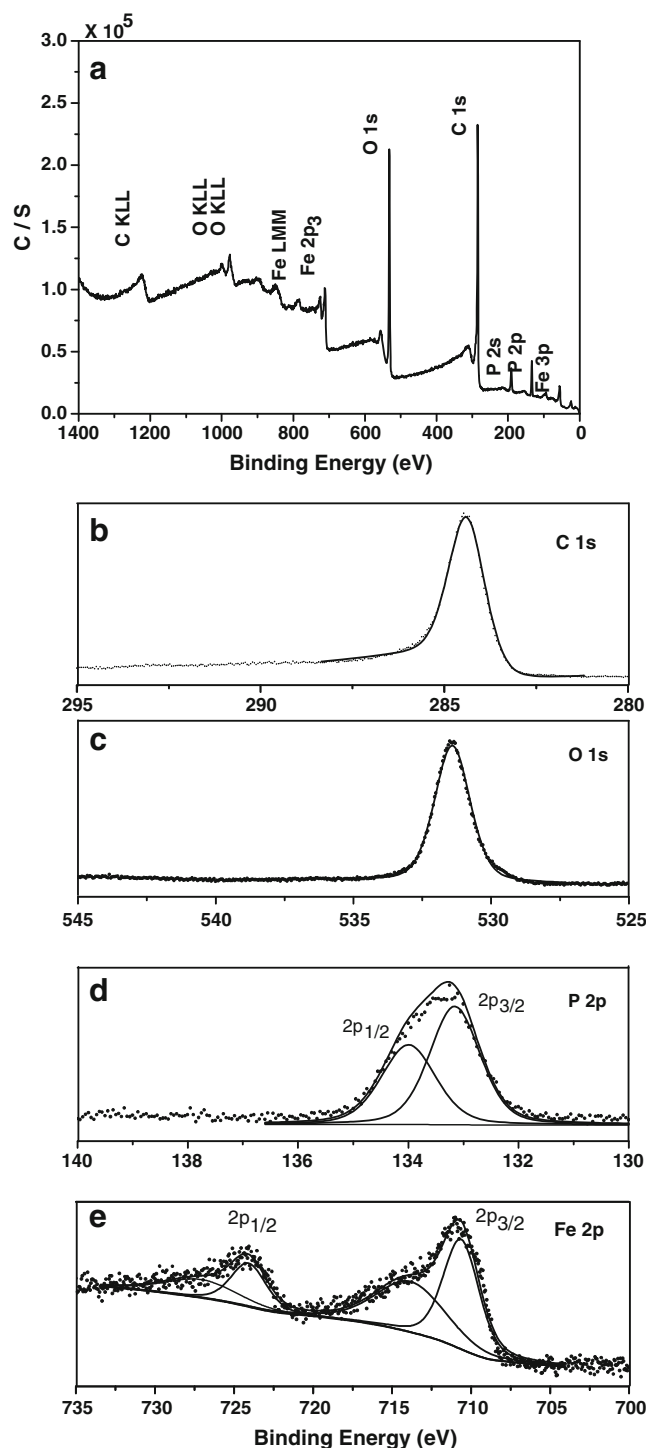

Fig. 2 **a** The full XPS spectrum for sample B; **b** C 1 s, O 1 s, P 2p and Fe 2p core spectra for sample B. The *solid lines* represent the individual peaks and the total fit. The experimental data are represented by *dots*

favorable to achieve unhindered contract of electrolyte with particle's exterior. Sample C (Fig. 3c) displays the spherical aggregates of crystallites about 64 nm, but the
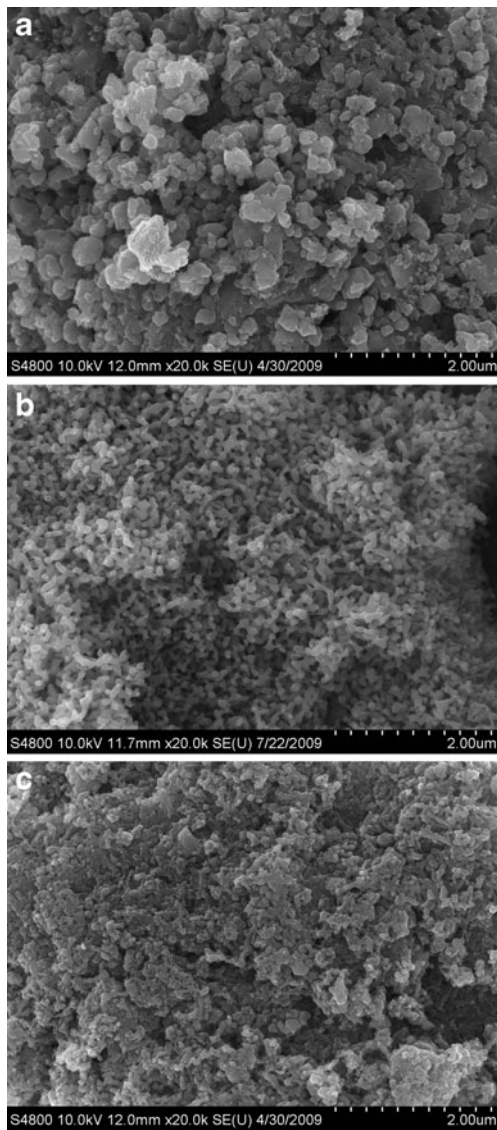
Fig. 3 FESEM photographs of the different LiFePO$_4$/C samples synthesized at 923 K for 15 h. **a** Sample A; **b** Sample B; **c** Sample C

dispersion of particles is evidently not as good as that of the sample B. The results indicate that the presence of the residual carbon is actually beneficial to refine the particle size. However, the higher level of the residual carbon content might bring a negative effect on dispersion of nanoparticles, which is not conducive to full infiltration of electrolyte.

Figure 4 shows HR-TEM images of different LiFePO$_4$/C composite samples. The straight line region represents LiFePO$_4$ crystallites and the wave form region refers to the amorphous carbon. As shown in Fig. 4a–c, the lattice fringes correspond to the (211), (121) and (111) lattice planes of olivine LiFePO$_4$, respectively. It is revealed from the HR-TEM image that a uniform layer of amorphous
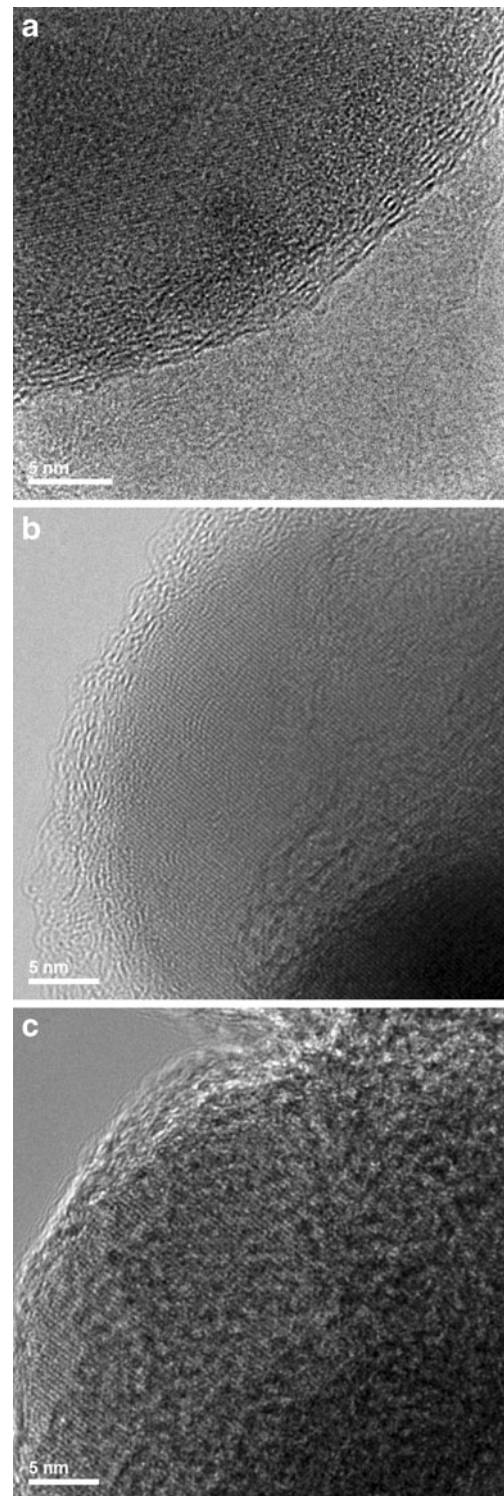
Fig. 4 HR-TEM images of **a** Sample A, **b** Sample B and **c** Sample C

carbon was coated on the surface of the LiFePO$_4$ nanoparticles as expected. The thickness of carbon coated ranges from 2.1, 3.3 to 4.5 nm with the increase in residual carbon amounts.

Electrochemical characterizations

The dependency of the galvanostatic discharge performances on the residual carbon amount at different C rates from 0.1 to 10 C between 2.5 V and 4.2 V verse Li are investigated as shown in Fig. 5. At all C rates, the samples show similar discharge curves. The flat part corresponds to the two-phase reaction of $LiFePO_4$ and $FePO_4$ meanwhile the sloped ones at the beginning and the end refer to the activation and concentration polarizations, respectively. Additionally, it could be noted that the constant voltage profiles of the discharge curves for all samples dropped from 3.42 to 3.24 V as the current density increased. Moreover, the discharge capacities fell off with increasing discharge C rate. However, several apparent differences could be easily found out. First, at a low rate of 0.1 C (0.085 mA), sample A delivered a specific capacity of 127 mA hg^{-1}. Sample B exhibited a higher specific capacity of approximately 162.7 mA hg^{-1}. These disparities in specific capacities between them mainly result from the differences in electronic conductivities. The poor electrical conductivity will limit the electron transport among particles and thus greatly hinders the intercalation/deintercalation of lithium-ion. This negative factor would lead to end prematurely the charge/discharge process and make the discharge capacity on the low side. But surprisingly, the sample C with the highest electrical conductivity showed a slight decrease of the specific capacity, around 158.1 mA hg^{-1}. It might be relevant to the microstructure of the sample C. The poor dispersion of nanoparticles might undermine the lithium ion diffusion and thus give rise to decreasing the specific capacity. Second, with the increase of the current density, the sample A exhibits worse capacity retention. The wider size distribution goes against the enhancement of the high-current charge and discharge performance. During the charge and discharge process, the smaller particles firstly fill or deplete up while the core of the larger particles are not fully utilized. As a result, the sample A shows lower discharge capacities at all C rates. As mentioned above, the sample C displays highest specific surface area, smallest particle size and highest electrical conductivity which are advantageous factors to enhance electrochemical capability of electrode materials, especially at the high current. The high specific surface area increases the diffusion effective area of lithium ion. The small particle size shortens the distance of lithium ion diffusion within the particles. Thus, it is expected that the sample C will exhibit most excellent electrochemical performances, even at the higher current density. However the measured results are completely different from our expectation. It showed a rapid capacity fading with the increase of C rate. This abnormal phenomenon mainly lies in the microstructure of material.
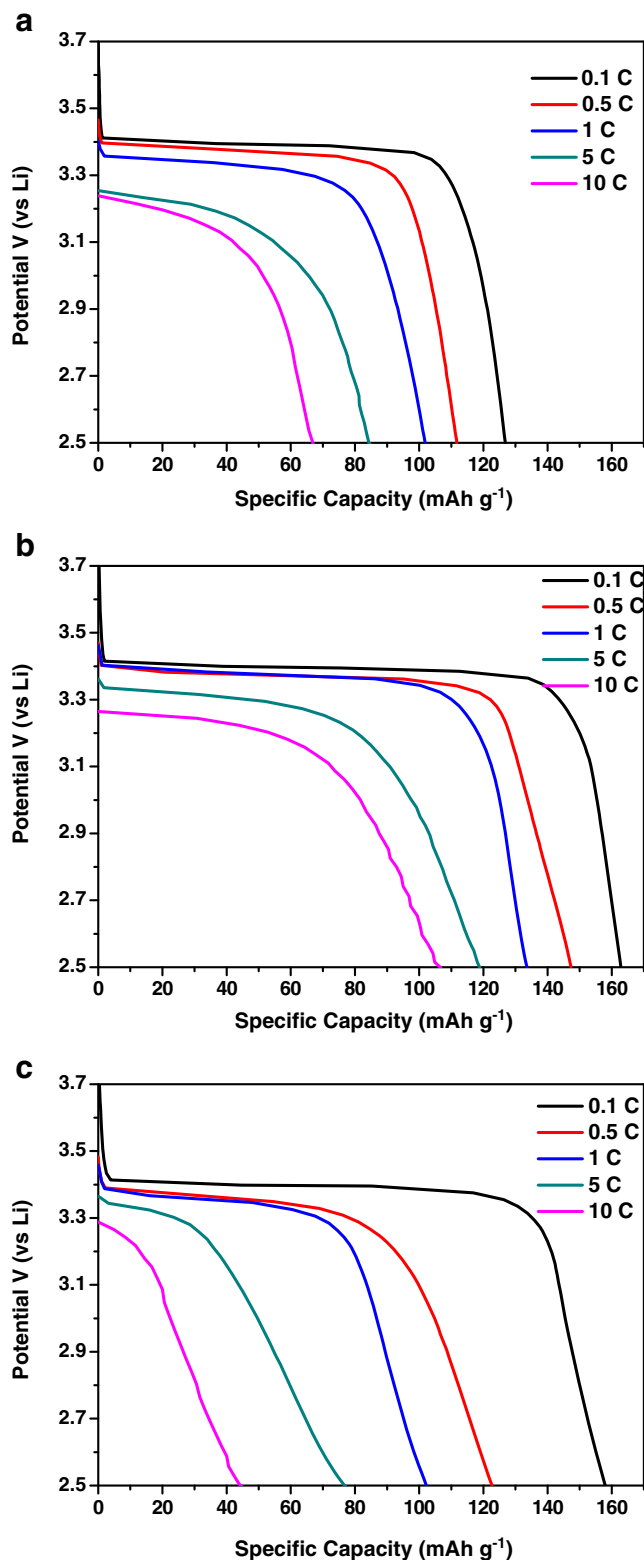

Fig. 5 The voltage profile recorded during discharge vs. specific capacity at different C rates from 0.1 to 10 C for the different $LiFePO_4$/C composite materials prepared. **a** Sample A; **b** Sample B; **c** Sample C
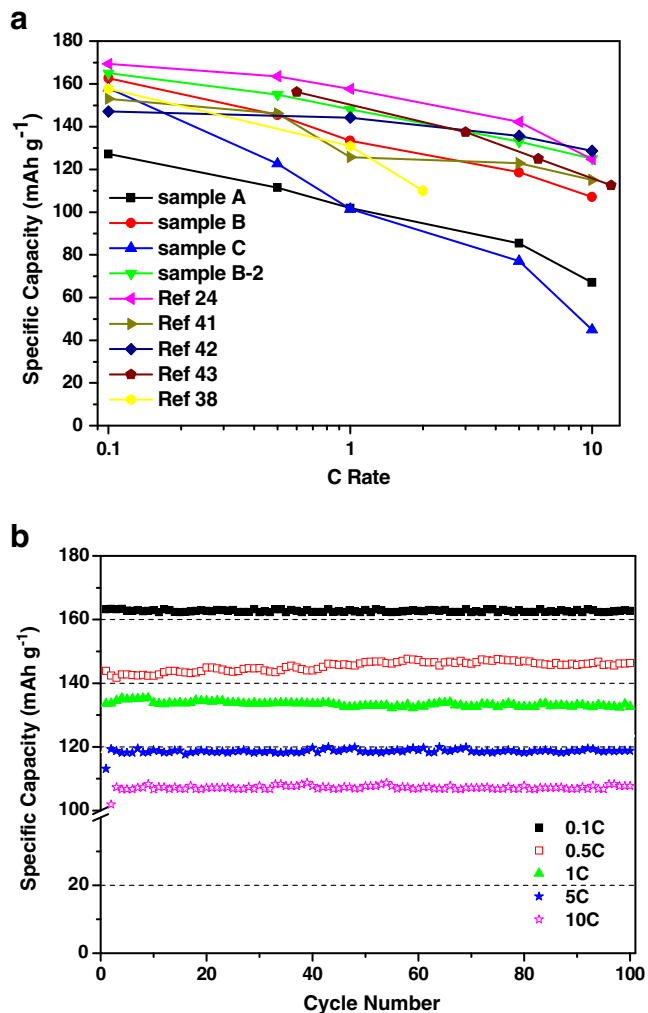
Fig. 6 **a** The rate capability of the LiFePO$_4$/C electrode with different residual carbon amounts compared with some results in the literature. **b** The discharge specific capacity retention vs. the cycle number for sample B scanned between 0.1 and 10 C

was found to show better rate capability than that of samples A and C. It would seem that the rate capability of sample B is more inferior to the others. This is not the case, however. Usually, the amount of the conductive carbon added is not less than 10 wt.% for preparing the cathode, whereas only 5 wt.% super P is added here. When the added amount of the conductive carbon (super P) was increased to 10 wt.% (labeled as sample B-2), it was observed that the rate capability of sample B is superior to that reported by Qian et al. [41] and Li et al. [38]. Although the more conductive carbon was added for preparing the cathode, the rate performance of LiFePO$_4$ reported by Zhou et al. [42] is still poorer than that of sample B as the C rate is less than 5 C. And under the higher rate (>5 C), the capacity delivered is basically the same as that of sample B. In addition, the LiFePO$_4$ powder synthesized by Wang et al. [43] are 36 nm nanoparticles with a specific BET surface of
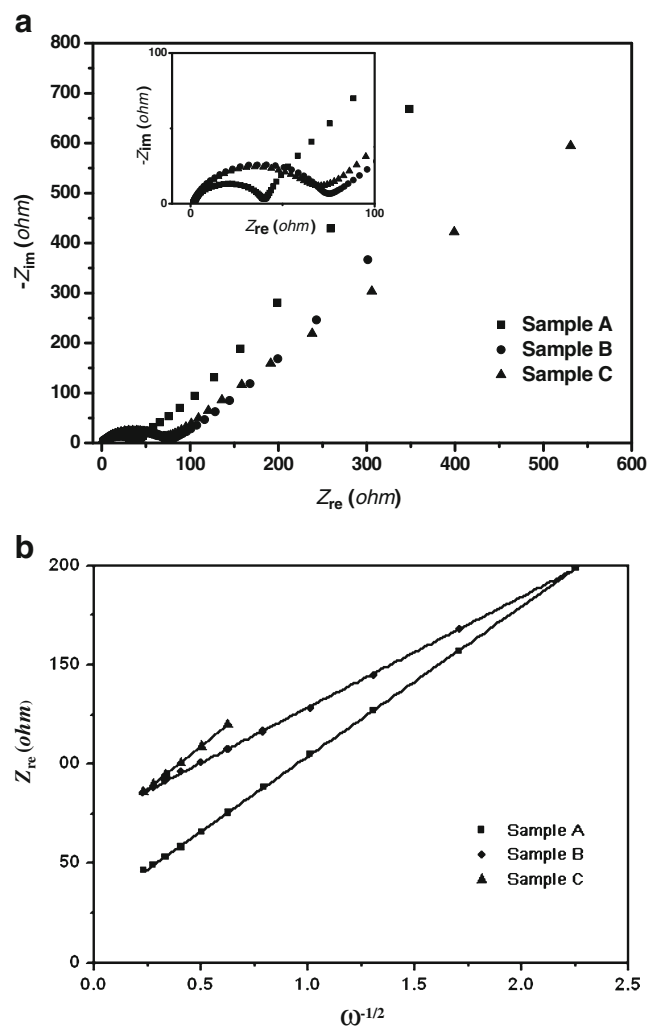

Fig. 7 **a** The Nyquist plots of the different LiFePO$_4$/C samples in the frequency range between 10 mHz and 100 kHz. **b** The relationship between Z_{re} and $\omega^{-1/2}$ at low frequency

The poor dispersion might prevent nanoparticles from soaking with the electrolyte. On the other hand, too much amorphous carbon around particles would block the transport channels of lithium-ion or generate an additional resistance to Li$^+$ diffusion between the surface of particles and electrolyte. It would be confirmed by EIS measurement described later. These two negative factors would greatly deteriorate the electrochemical performances at the high C rates. Therefore, we could make a conclusion that the electrochemical responses of electrode materials in fact are a coupled result of electrical conductivity, particles size, size distribution and microstructure. This fully explains why sample B shows most excellent electrochemical performances, although it exhibits lower electrical conductivity and larger particle size as compared with sample C.

Figure 6a lists the rate capability of the as-synthesized samples compared with typical literature results. Sample B

50 m^2 g^{-1}, whereas the particle size of the sample B is about 49 nm and the specific surface area is approximately 35 m^2 g^{-1}. Nonetheless, sample B still exhibits more excellent rate performance at higher C rates (>5 C). However, the rate performance of sample B is inferior to some extent to that reported by Choi [24]. The leading reason might be that the active material loading amount is between 2.1 and 2.6 mg cm^{-2} reported by Choi, whereas that of sample B is about 5 mg cm^{-2}, which is likely to limit the transport of Li$^+$ into the electrode. On the other hand, the cut-off potential (from 2.0 to 4.5 V) measured is wider than that used here. In fact, the electrochemical performance of sample B is more likely to have an advantage over that reported by Choi [24]. Therefore, it can be regarded that the nanostructured LiFePO$_4$/C electrode with more excellent rate capability could be successfully synthesized by this inorganic sol–gel approach.

Figure 6b shows the cycling stability at the different C rates for sample B. It was found that at all C rates, cycling behavior was quite stable. At 0.1 C (0.085 mA), the discharge capacity is close to the theoretical value. At 0.5 C (0.425 mA), the discharge capacity gradually increases with cycling. And specific capacities of 119 and 108 mA h g^{-1} were recorded after the 100th cycle at 5 C (4.25 mA) and 10 C (8.5 mA), respectively. The excellent cycling stability again indicates the important role of the electrical conductivity, particle size, size distribution and microstructure in determining the electrochemical performances.

Figure 7a shows Nyquist plots for three samples under open-circuit condition. All plots exhibited a depressed semicircle in high-frequency region and a skew line in a very low-frequency region. The diameter of the depressed semicircle on the Z_{re} axis is approximately R_{ct} (the charge transfer resistance). The amorphous carbon outside of particles hinders the transfer of lithium-ion from the electrolyte to the particle's exterior and will finally lead to the increase of R_{ct}. Thus, as the residual carbon content increased, R_{ct} increased gradually. In addition, the distortion in impedance circle became more pronounced upon the remaining carbon content. The serious distortion might mainly depend on the high double-layer capacitance which originates from the amorphous carbon surrounding the particles. The results are in good agreement with the residual carbon amounts. The skew line at very low frequencies was closely related to the lithium ion diffusion in the cathode active material, also called the Warburg diffusion. The lithium ion diffusion coefficient could be calculated using equation [44] $D = R^2T^2/2A^2n^4F^4C^2\sigma^2$, where R is the gas constant (8.314 JK^{-1} mol^{-1}), T is the absolute temperature, A is the specific surface area of the cathode, n is the number of electron per molecule participated in the redox reaction, F is the Faraday constant (96,480 Cmol^{-1}), C is the concentration of lithium ion

(0.02278 mol cm^{-3}) and σ is the Warburg factor determined by the equation $Z_{re} = R_D + R_L + \sigma\omega^{-1/2}$.

Figure 7b shows plots of Z_{re} as a function of the reciprocal square root of ω for three different samples. Through substitution of σ, the diffusion coefficients of lithium ion were calculated as 1.60×10^{-12}, 1.66×10^{-12} and 2.57×10^{-13} cm^2 s^{-1}, respectively. From the aspect of dynamic, the results confirmed that the thicker carbon coating might be detrimental to lithium ion transfer, although it played a positive role in increasing the bulk electrical conductivity and refining the particle size. At the same time, from the dynamic point of view, the results explained well why sample B displayed excellent performance and cycling behavior.

Conclusions

The pure and nanostructured LiFePO$_4$/C composite powder was synthesized using low-cost and environmental benign inorganic compounds combination via a simplified sol–gel route. The dependency of the physicochemical and electrochemical performances on the remaining carbon amount was investigated in details. The presence of the residual carbon plays a positive role in reducing the particle size, optimizing microstructure and increasing bulk electrical conductivity. However, amorphous carbon layer might hinder lithium ion transport between the electrolyte and particles. Therefore, by optimizing the residual carbon content, an excellent electrochemical performance could be achieved. When the residual carbon amount was about 4.5 wt.%, the sample shows a porous and loose microstructure formed by spherical particles with a size of ~71 nm. This unique morphology allows the material to exhibit high specific capacity, excellent rate performance and stable cycling stability.

References

1. Broussely M, Perton F, Biensan P, Bodet JM, Labat J, Lecerf A, Delmas C, Rougier A, Pérès JP (1995) J Power Sources 54 (1):109–114
2. Thackeray MM, Johnson PJ, De Picciotto LA, Bruce PG, Goodenough JB (1984) Mater Res Bull 19(2):179–187
3. Padhi AK, Nanjundaswarmy KS, Goodenough JB (1997) J Electorchem Soc 144:1188–1194

4. Eills B, Subramanya Herle P, Rho YH, Nazar LF, Dunlap R, Perry LK, Ryan DH (2007) Faraday Symp Chem Soc 34:119–141
5. Andersson AS, Kalska B, Häggström L, Thomas JO (2000) Solid State Ionics 130:41–52
6. Giorgetti M, Berrettoni M (2006) Inorg Chem 45:2750–2757
7. Prosini PP, Lisi M, Zane D, Pasquali M (2002) Solid State Ionics 148:45–51
8. Chen JM, Hsu CH, Lin YR, Hsiao MH, Fey GTK (2008) J Power Sources 184:498–502
9. Wang GX, Yang Y, Chen JZ, Beylay S, Liu HK (2005) Electrochim Acta 50:4649–4654
10. Sung WO, Seung TM, Seung MH, Oh S-M, Oh KH, Amine K, Scrosati B, Sun YK (2010) Adv Mater 22:4842–4845
11. Zhao JQ, He JP, Zhou JH, Guo YX, Wang T, Wu SC, Ding XC, Huang RM, Xue HR (2011) J Phys Chem C 115:2888–2894
12. Sides CR, Croce F, Yong VY, Martin CR, Scrosati B (2005) Electrochem Solid-State Lett 8:A484–A487
13. Yang M, Gao QM (2011) J Alloys Compd 509:3690–3698
14. Dimesso L, Jacke S, Spanheimer C, Jaegermann W (2011) J Alloys Compd 509:3777–3782
15. Yamada A, Kudo Y, Liu KY (2001) J Electrochem Soc 148(10):A1153–A1158
16. Chung SY, Bloking JT, Chiang YM (2002) Nat Mater 1:123–128
17. Yang MR, Ke WH (2008) J Electrochem Soc 155(10):A729–A732
18. Meethong N, Kao YH, Speakman SA, Chiang YM (2009) Adv Funct Mater 19:1060–1070
19. Arumugam D, Paruthimal KG, Manisanker P (2009) J Solid State Electrochem 13:301–307
20. Sun CS, Zhou Z, Xu ZG, Wang DG, Wei JP, Bian XK, Yan J (2009) J Power Source 193:841–845
21. Yang L, Jiao LF, Miao YL, Yuan HT (2009) J Solid State Electrochem 13:1541–1544
22. Sun CS, Zhang Y, Zhang XJ, Zhou Z (2010) J Power Source 195:3680–3683
23. Liao XZ, He YS, Ma ZF, Zhang XM, Wang L (2007) J Power Source 174:720–725
24. Choi D, Kumta PN (2007) J Power Sources 163:1064–1069
25. Seung AH, Su JK, Jaehoo K, Chung KY, Cho B-W, Kang JW (2010) J Supercrit Fluids 55:1027–1037
26. Gómez LS, Meatza ID, Martín MI, Bengoechea M, Cantero I, Rabanal ME (2010) Electrochim Acta 55:2805–2809
27. Mestre AF, Hamelet S, Mascquerlier C, Palacin MR (2010) J Power Sources 195:6897–6901
28. Sabina B, Libero D, Marina M (2008) J Power Sources 180:875–879
29. Liu HP, Wang ZX, Li XH, Guo HJ, Peng WJ, Zhang YH, Hu QY (2008) J Power Sources 184:469–472
30. Liu YY, Cao CB (2010) Electrochim Acta 55:4694–4699
31. Zhecheva E, Mladenov M, Zlatilova P, Koleva V, Stoyanova R (2010) J Phys Chem Solids 71:848–853
32. Beninati S, Damen L, Mastragostino M (2008) J Power Source 180:875–879
33. Sanchez MAE, Brito GES, Fantini MCA, Goya GF, Matos JR (2006) Solid State Ionics 177:497–500
34. Kuwahara A, Suzuki S, Miyayama M (2010) J Electroceram 24:69–75
35. Kim J-K, Choi J-W, Chauhan GS, Ahn J-H, Hwang GC, Choi JB, Ahn H-J (2008) Electrochim Acta 53:8258–8264
36. Sundarayya Y, Kumara Swamy KC, Sundana CS (2007) Mater Res Bull 42:1942–1948
37. Croce F, Epifanio AD, Hassoun J, Deptula A, Olczac T, Scrosati B (2002) Electrochem Solid-State Lett 5(3):A47–A50
38. Li XL, Wang WD, Shi CW, Wang H, Xing Y (2009) J Solid State Electrochem 13:921–926
39. Bewlay SL, KonstantinoV K, Wang GX, Dou SX, Liu HK (2004) Mater Lett 58(11):1788–1791
40. Bhuvaneswari MS, Bramink NN, Ensling D, Ehrenberg H, Jaegermann W (2008) J Power Sources 180:553–560
41. Qian JG, Zhou M, Cao YL, Ai XP, Yang HX (2010) J Phys Chem 114:3477–3482
42. Zhou XF, Wang F, Zhu YM, Liu ZP (2011) J Mater Chem 21:3353–3358
43. Wang YG, Wang YR, Hosono E, Wang KX, Zhou HS (2008) Angew Chem Int Ed 47:7461–7465
44. Bard AJ, Faulkner LR (2001) Electrochemical methods, 2nd edn. Wiley, New York, p 231